

Compressible Taylor–Couette flow – instability mechanism and codimension 3 points

Stephanie Welsh, Evy Kersalé† and Chris A. Jones

Department of Applied Mathematics, University of Leeds, Leeds LS2 9JT, UK

(Received 10 January 2013; revised 4 April 2014; accepted 15 May 2014;
first published online 10 June 2014)

Taylor–Couette flow in a compressible perfect gas is studied. The onset of instability is examined as a function of the Reynolds numbers of the inner and outer cylinder, the Mach number of the flow and the Prandtl number of the gas. We focus on the case of a wide gap, with radius ratio 0.5. We find new modes of instability at high Prandtl number, which can allow oscillatory axisymmetric modes to onset first. We also find that onset can occur even when the angular momentum increases outwards, so that the classical Rayleigh criterion can be violated in the compressible case. We have also considered the case of counter-rotating cylinders, where the $m = 0$ and $m = 1$ modes can onset simultaneously to give a codimension 2 bifurcation, leading to the formation of complex flow patterns. In compressible flow we also find codimension 3 points. The Mach number and the critical inner and outer Reynolds numbers can be adjusted so that the two neutral curves for the $m = 0$ and $m = 1$ modes touch rather than cross. Complex codimension 3 points occur more readily in the compressible case than in the Boussinesq case, and they are expected to lead to a rich nonlinear behaviour.

Key words: bifurcation, gas dynamics, Taylor–Couette flow

1. Introduction

Taylor–Couette flow, the flow found between two concentric rotating cylinders, has been much studied both theoretically and experimentally. In the vast majority of this work, the fluid has been assumed incompressible. The first successful analysis of the incompressible problem was done by Taylor (1923). However, his work focused on those cases where the difference of the radii of the cylinders is small. More comprehensive studies of the linear incompressible problem have since been done, for example by Chandrasekhar (1961) and Davey, DiPrima & Stuart (1968). However, most of the research effort in the incompressible case has been focused on experimental problems.

The present paper was originally motivated by astrophysical questions and we have thus concentrated our efforts on the compressible problem. A major challenge in astrophysical fluid dynamics has been to explain the turbulence which must be present in accretion disks. Since the angular momentum increases outwards in disks in Keplerian rotation one might naively expect these disks to be stable. Magnetorotational instability has been identified as a possible solution to the problem of turbulence and

† Email address for correspondence: E.Kersale@leeds.ac.uk

angular momentum transport in accretion disks (Balbus & Hawley 1998), though purely hydrodynamic explanations have also been considered (see e.g. Armitage 2011, and references therein). Similarities between astrophysical disks and fluid flows bounded by concentric differentially rotating cylinders have motivated a number of theoretical and experimental studies of hydrodynamic and magnetohydrodynamic Taylor–Couette flows (see, e.g. Goodman & Ji 2002; Dubrulle *et al.* 2005; Hersant, Dubrulle & Huré 2005; Stefani *et al.* 2006). One problem of considerable interest is, for instance, the controversial question of subcritical hydrodynamic turbulence in Keplerian-like Taylor–Couette flows. From the experimental measurement of the torques acting on the cylinders Paoletti & Lathrop (2011) found that efficient angular momentum transport would be possible in accretion disks for purely hydrodynamical reasons; this is in contradiction with experiments conducted by Ji *et al.* (2006) who demonstrated that the required turbulence level could not be achieved in their apparatus. There is still no consensus on this issue despite subsequent complementary experimental runs (Paoletti *et al.* 2012; Schartman *et al.* 2012). As yet, no studies of Taylor–Couette flows motivated by astrophysical problems have considered the effects of compressibility, despite the fact that accretion disk flows have high Mach numbers.

To date, the only controlled laboratory experiment on compressible Taylor–Couette flow was reported by Larignon, Marr & Goldstein (2006) who went up to Mach 2. At these speeds the Reynolds number is too far above critical to make contact with linear theory unless the gas density is very low, to compensate for the low value of the dynamic viscosity (see (2.6) below). Their experiment was therefore carried out in a low pressure environment of 10–100 Pa. They used a narrow gap apparatus, and measured the torque and the heat flux and compared their results with numerical simulations assuming axisymmetry. At the lowest pressures, their results were consistent with laminar flow, but at the higher pressures, where the Reynolds number was beyond the critical value, they were consistent with a Taylor-vortex flow. Their heat flux measurements suggested that significant heat is being generated in the fluid interior. It is slightly surprising that so little experimental work has been done on the compressible problem, as huge advances were made in fluid mechanics from the experimental and theoretical studies of the incompressible problem.

The compressible Taylor–Couette problem becomes somewhat more complex with an added equation of state and a temperature equation. A sensible choice of boundary conditions, particularly for the density ρ , also requires some care. So far, the problem has been relatively neglected, with only a few studies published. Hatay *et al.* (1993) concluded that compressibility has a stabilising effect, while Kao & Chow (1992) found that compressibility both stabilises and destabilises, depending on the temperature ratio and speeds of the cylinders. In response to this paper, Manela & Frankel (2007) published another study which focuses particularly on the narrow gap limit and they conclude that compressibility stabilises. They pointed out that some previous studies had not conserved mass as the external parameters were varied. They have also modified the no-slip boundary condition to allow for a very low density fluid where the mean free path is comparable to the gap-width. This is a regime of interest for potential experiments, but here we use the classical continuum approximation.

In this paper we concentrate on two aspects of the problem which have revealed what we believe to be new phenomena. The first area investigated is the stability of axisymmetric disturbances. We have explored a much greater range of space than in previous studies. At Prandtl number unity and with the outer cylinder stationary, we find that compressibility is generally stabilising, in agreement with Manela & Frankel

(2007). However, at higher Prandtl numbers, we find new branches of instability. Somewhat surprisingly, we can even find instability below the Rayleigh line (see e.g., Chandrasekhar 1961), that is when the angular momentum increases outwards. Even at moderate Prandtl numbers, in compressible flow the Rayleigh criterion can be violated. Another surprising phenomenon is that there are significant regions of the parameter space where axisymmetric modes first onset in oscillatory form, that is, through a Hopf bifurcation. This cannot happen with an incompressible fluid (Yih 1972).

The second aspect we examined was the counter-rotating case, where it is known that $m = 1$ non-axisymmetric modes may onset before axisymmetric $m = 0$ modes, and at special codimension 2 points, the two modes can onset simultaneously. This leads to interesting and rich nonlinear behaviour; see e.g. Chossat & Iooss (1994). They are called codimension 2 points because two parameters, often the Reynolds numbers of the outer cylinder and inner cylinder, must have particular values for the simultaneous onset. In the compressible problem, we find not only these codimension 2 points but also codimension 3 points. Normally, the curves of critical inner Reynolds number as a function of outer Reynolds number for the $m = 0$ and $m = 1$ modes cross at the codimension 2 point. At certain values of the Mach number these curves touch rather than cross, giving rise to a codimension 3 point. This phenomenon requires three parameters to be tuned to specific values, and below these are taken to be the two Reynolds numbers and the Mach number.

This codimension 3 behaviour can occur in the incompressible case (Signoret 1988; Signoret & Iooss 1988) at low radius ratio, but it appears to be much more common in the compressible case. We have not explored here the nonlinear behaviour associated with these codimension 3 points. Other examples in the literature suggest that many different possibilities can occur, so this will be a substantial further undertaking, beyond the scope of this paper.

2. Governing equations

We consider two infinite, concentric cylinders of radius R_1 and R_2 , with $R_2 > R_1$ where $d = R_2 - R_1$ is the gap width between them. We use cylindrical coordinates (r, θ, z) where z coincides with the common axis of the cylinders. The gap is filled with a compressible fluid of density ρ , pressure p and temperature T . The fluid is maintained at constant temperature on both inner and outer cylinders. However, viscous heating, Φ , produced by the fluid flow $\mathbf{u} = (u_r, u_\theta, u_z)$ leads to the interior fluid having a higher temperature than the boundaries.

We consider a fluid with constant dynamic viscosity, $\hat{\mu}$, coefficient of thermal conduction, \hat{k} , and specific heats, c_p and c_v . As a result of mass density variations, the fluid kinematic viscosity $\nu = \hat{\mu}/\rho$ and thermal diffusivity $\kappa = \hat{k}/(\rho c_p)$ are not constant. The temperature dependence of $\hat{\mu}$ and \hat{k} observed in kinetic models of compressible fluids has therefore not been considered in our study. However, in order to get some insights into the effects of nonuniform transport coefficients on the dynamics of the flow, we have also partially investigated the case of constant ν and κ , which has led to qualitatively similar results. Since the equations governing both regimes of dissipation are conceptually close but somewhat different, we only present in this paper results obtained for constant $\hat{\mu}$ and \hat{k} ; the main differences between the two regimes will however be emphasised. For simplicity, we also assume that the fluid is a perfect gas of adiabatic index $\gamma = c_p/c_v$, which is taken as $\gamma = 5/3$. We neglect gravity, which will be small in comparison with the centrifugal acceleration at the high rotation rates we envisage.

The two cylinders are maintained at constant angular velocities and we examine the resulting fluid flow, governed by the equations

$$\frac{\partial \rho}{\partial t} + \nabla \cdot (\rho \mathbf{u}) = 0, \tag{2.1}$$

$$\rho \left(\frac{\partial \mathbf{u}}{\partial t} + \mathbf{u} \cdot \nabla \mathbf{u} \right) = -\nabla p + \nabla \cdot (2\hat{\mu} \mathbf{e}) - \frac{2}{3} \nabla (\hat{\mu} \nabla \cdot \mathbf{u}), \tag{2.2}$$

$$\rho c_v \left(\frac{\partial T}{\partial t} + \mathbf{u} \cdot \nabla T \right) = -p \nabla \cdot \mathbf{u} + \nabla \cdot (\hat{k} \nabla T) + \Phi, \tag{2.3}$$

$$\Phi = \hat{\mu} \left(2e_{ij}e_{ij} - \frac{2}{3} (\nabla \cdot \mathbf{u})^2 \right) \quad \text{where } e_{ij} = \frac{1}{2} \left(\frac{\partial u_i}{\partial x_j} + \frac{\partial u_j}{\partial x_i} \right), \tag{2.4}$$

$$p = (c_p - c_v) \rho T. \tag{2.5}$$

2.1. Nondimensional equations

Let M_0 be the mass per unit length of fluid between the two cylinders. The unit of length is the gap width, d , and the unit of mass density the average fluid density within the gap, $\rho_* = M_0 / (\pi(R_2^2 - R_1^2))$, or equivalently the density of an incompressible fluid of the same mass. Some previous studies (e.g. Kao & Chow 1992; Hatay *et al.* 1993) used ρ at the inner boundary as the unit of density but, as noted by Manela & Frankel (2007), only M_0 can be prescribed in experiments, not the local density; in our equilibrium models, ρ can vary quite significantly at the inner cylinder as the parameters change. The unit of time is the viscous relaxation time, $\rho_* d^2 / \hat{\mu}$, $\hat{\mu}$ constant, and the unit of temperature, T_* , the temperature on the inner cylinder. This leads to the units of velocity $\hat{\mu} / (\rho_* d)$ and pressure $(c_p - c_v) \rho_* T_*$.

The ratio of the angular velocity of the outer cylinder to the angular velocity of the inner cylinder is defined by $\mu = \Omega_2 / \Omega_1$ and $\eta = R_1 / R_2$ is the radius ratio, which is taken as $\eta = 0.5$ in the calculations described in this paper, except in a few cases which are detailed below. These are familiar definitions from the incompressible case. We also introduce Re_1 , the Reynolds number at the inner cylinder, and Re_2 , the Reynolds number at the outer cylinder:

$$Re_1 = \frac{\Omega_1 R_1 \rho_* d}{\mu}, \quad Re_2 = \frac{\Omega_2 R_2 \rho_* d}{\mu}. \tag{2.6a,b}$$

The isothermal sound speed c_s is given by $c_s^2 = (c_p - c_v) \rho_*^2 T_* d^2 / \hat{\mu}^2$ and is a dimensionless parameter, but it is more convenient to define the Mach number $Ma = Re_1 / c_s$ which is a useful measure of compressibility. The limit $Ma \rightarrow 0$ is the incompressible limit in which we expect to recover the well-known Boussinesq results.

Once the pressure, $p = \rho T$, is eliminated, the dimensionless equations become

$$\frac{\partial \rho}{\partial t} + \nabla \cdot (\rho \mathbf{u}) = 0, \tag{2.7}$$

$$\rho \left(\frac{\partial \mathbf{u}}{\partial t} + \mathbf{u} \cdot \nabla \mathbf{u} \right) = -\frac{Re_1^2}{Ma^2} \nabla (\rho T) + \nabla^2 \mathbf{u} + \frac{1}{3} \nabla (\nabla \cdot \mathbf{u}), \tag{2.8}$$

$$\rho \left(\frac{\partial T}{\partial t} + \mathbf{u} \cdot \nabla T \right) = -(\gamma - 1) \rho T \nabla \cdot \mathbf{u} + \frac{\gamma}{Pr} \nabla^2 T + (\gamma - 1) \frac{Ma^2}{Re_1^2} \Phi, \tag{2.9}$$

where $Pr = c_p \hat{\mu} / \hat{k}$ is the Prandtl number.

The boundary conditions are taken as no-slip, with constant temperature boundaries,

$$\begin{aligned}
 u_r = 0, \quad u_z = 0 \quad \text{on } r = \frac{\eta}{1-\eta}, \quad r = \frac{1}{1-\eta}; \\
 u_\theta = Re_1, \quad T = 1 \quad \text{on } r = \frac{\eta}{1-\eta}; \\
 \text{and } u_\theta = Re_2, \quad T = \chi \quad \text{on } r = \frac{1}{1-\eta}.
 \end{aligned}
 \tag{2.10}$$

The outer cylinder temperature is always taken as $\chi = 1$ unless otherwise stated. Manela & Frankel (2007) used a set of boundary conditions which introduces additional kinetic effects. The dynamical and thermal importance of these processes is quantified by the Knudsen number, Kn , defined as the ratio of the mean free path to the gap width. Using the kinetic theory of a perfect gas, which relates the viscosity to the mean free path, we obtain $Kn \sim Ma/Re_1$ with a constant of proportionality of order unity. Yoshida & Aoki (2006) found that centrifugal instabilities are suppressed for $Kn \gtrsim 0.01$ in Taylor–Couette flows of rarefied gases, for a limited domain of the parameter space. Their calculations showed a good agreement between the Bhatnagar–Gross–Krook model of kinetic theory and the continuum model, except when large mass density gradients are present. Here we typically expect $Kn < 0.01$, so that the continuum limit applies, except in some particular circumstances, e.g. for large Mach numbers or high Prandtl numbers.

The basic state solutions of (2.7)–(2.12), denoted by ρ_0 , u_0 and T_0 , where u_0 consists of a purely azimuthal flow, are functions of r only. We linearise for small perturbations about the basic state, seeking normal modes of the form $\sim \exp(\sigma t + im\theta + ikz)$, where m is the azimuthal wavenumber, k is the axial wavenumber and σ is in general complex. The linear equations are reduced to scalar equations, details being given in appendix A.

2.2. The basic state

As in Boussinesq Couette flow, we seek a basic state solution with $u_r = u_z = 0$ and steady axisymmetric azimuthal flow. The solution of the θ -component of the momentum equation (2.8) is given by

$$u_\theta = Ar + \frac{B}{r}.
 \tag{2.11}$$

Following Chandrasekhar (1961),

$$A = Re_1 \frac{\mu - \eta^2}{\eta(1 + \eta)} \quad \text{and} \quad B = Re_1 \frac{\eta(1 - \mu)}{(1 - \eta)(1 - \eta^2)},
 \tag{2.12a,b}$$

where μ and η are defined in § 2. For the steady state temperature, we solve

$$\frac{1}{r} \frac{d}{dr} \left(r \frac{dT_0}{dr} \right) + \frac{\gamma - 1}{\gamma} \frac{Pr Ma^2}{Re_1^2} \left[r \frac{d}{dr} \left(\frac{u_\theta}{r} \right) \right]^2 = 0,
 \tag{2.13}$$

and obtain

$$T_0 = \chi + \frac{\gamma - 1}{\gamma} \frac{Pr Ma^2}{Re_1^2} B^2 \left(C \ln r - \frac{1}{r^2} + D \right) + (1 - \chi) \frac{\ln [r(1 - \eta)]}{\ln \eta},
 \tag{2.14}$$

where

$$C = \frac{(1 - \eta^2)(1 - \eta)^2}{\eta^2 \ln \eta} \quad \text{and} \quad D = (1 - \eta)^2 \left[1 + \frac{1 - \eta^2}{\eta^2} \frac{\ln(1 - \eta)}{\ln \eta} \right] \quad (2.15a,b)$$

are constants of integration.

The steady state density of mass is determined by the radial component of the momentum equation (2.8), which can be written as a second order boundary value problem for the distribution of mass defined by

$$M(r) = 2\pi \int_{\eta/(1-\eta)}^r \rho_0(s) s \, ds. \quad (2.16)$$

So, we first numerically solve the differential equation

$$\frac{d^2 M}{dr^2} + \left(\frac{1}{T_0} \frac{dT_0}{dr} - \frac{Ma^2}{Re_1^2} \frac{u_0^2}{r T_0} - \frac{1}{r} \right) \frac{dM}{dr} = 0, \quad (2.17)$$

with

$$M\left(\frac{\eta}{1-\eta}\right) = 0 \quad \text{and} \quad M\left(\frac{1}{1-\eta}\right) = \pi \frac{1+\eta}{1-\eta}, \quad (2.18a,b)$$

then we compute the mass density

$$\rho_0 = \frac{1}{2\pi r} \frac{dM}{dr}. \quad (2.19)$$

Our choice of unit of density ensures that the mass of fluid in the gap between the cylinders is a constant, but it also ensures consistency with the Boussinesq approximation since $\rho_0 \rightarrow 1$ as $Ma \rightarrow 0$.

There can be quite significant fluctuations in the density as Ma is increased, i.e. when the compressibility is increased. In figure 1, we show the basic state for a range of Ma at $Pr = 1$, $Re_2 = 0$ and Re_1 close to critical (see figure caption for the values of Re_1). At small Ma , i.e. the incompressible limit, the density is evenly distributed throughout the system. We notice that, as Ma increases, this profile changes dramatically and the density concentrates more and more towards the outer cylinder. This means, as compressibility increases, more of the mass in the system moves towards the outer cylinder and concentrates there, leaving less mass at the inner boundary. This behaviour is typical at moderate Prandtl number; however the distribution of mass within the gap can become even more complex as Pr increases (see figure 4). For this reason, we chose to fix the overall mass of fluid rather than the density at any specific point in the system.

Similarly, we notice that for small Ma , the temperature profile is fixed and there is almost no variation in the temperature. This is exactly what you would expect from the incompressible case, because for small Ma , the effect of viscous heating, Φ , is completely negligible. As Ma increases, we see the formation of a distinct hump. Indeed, the larger the increase in Ma , the more noticeable the hump becomes as the impact of Φ becomes more and more significant. The heat flux measurements in the experiment of Larignon *et al.* (2006) were consistent with the existence of a temperature hump in the interior of the fluid.

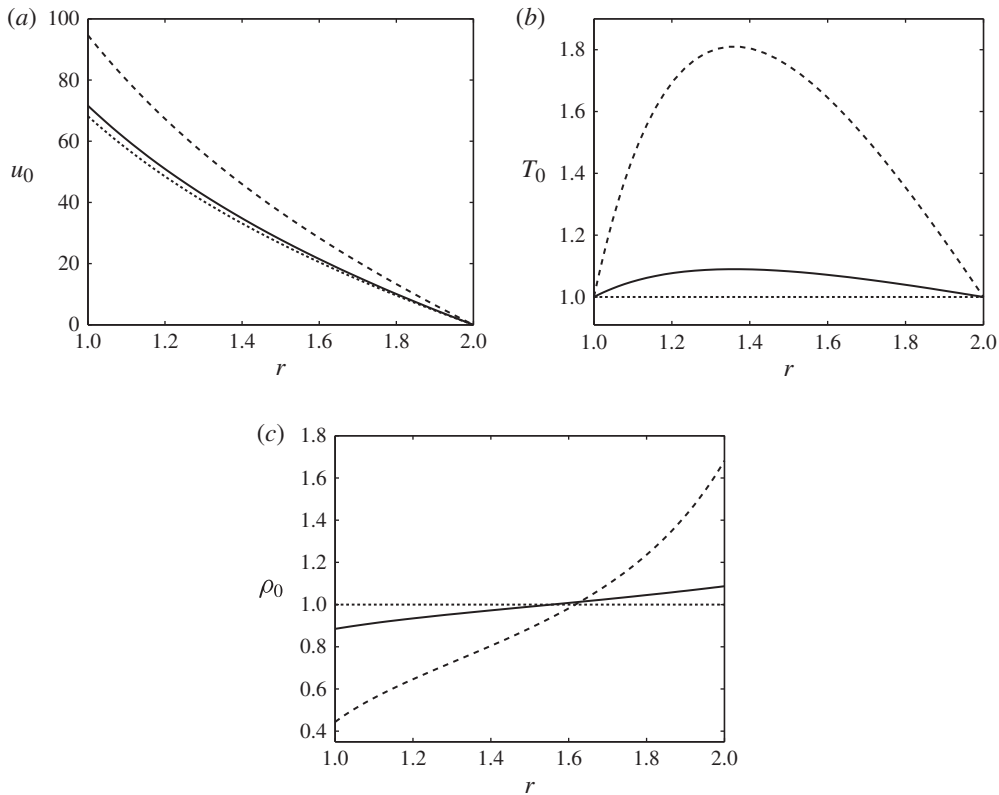


FIGURE 1. Basic state profiles of velocity (a), temperature (b) and density (c) for different values of Ma , with $Pr = 1$, $Re_2 = 0$ and Re_1 close to critical. The Mach number takes the following values: the incompressible case $Ma \approx 0$ with $Re_{1c} \approx 68.19$ (dotted line), $Ma = 1$ with $Re_{1c} \approx 71.64$ (solid line) and $Ma = 3$ with $Re_{1c} \approx 94.65$ (dashed line).

The steady state defined for constant $\hat{\mu}$ and \hat{k} by (2.11), (2.14) and (2.17) is the solution to a boundary value problem which consists of three second order differential equations for azimuthal velocity, temperature and radial mass distribution – the first two equations have been solved analytically, the third numerically. In the case of constant kinematic viscosity and thermal diffusion, steady states are solutions to an analogous boundary value problem, where the azimuthal velocity is still dictated by a vanishing viscous force in azimuth but since $\hat{\mu} = \rho\nu$ it now depends on the fluid mass density (see (2.2)); similarly, the heat conduction equation is now also a function of the density (see (2.3)). Thus, all three equations are coupled and require fully numerical solutions. In both regimes, we have found that the basic state temperature and mass distributions remain qualitatively similar for identical independent parameters, however an inflexion point appears in the azimuthal velocity profile as Pr is increased, when ν and κ are assumed constant.

3. Axisymmetric instabilities

We first consider modes with $m = 0$, because this is known to be the most unstable mode when $\mu = 0$ in the Boussinesq problem.

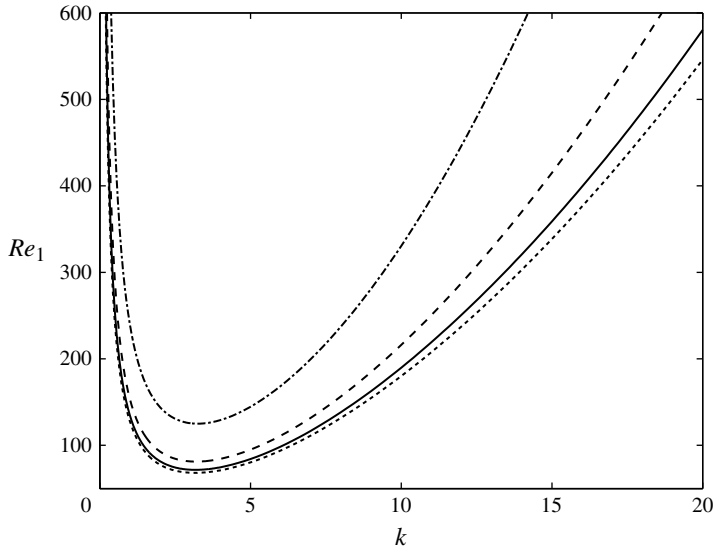


FIGURE 2. Curves of marginal stability showing Re_1 , at instability onset, vs k for $Pr = 1$, $Re_2 = 0$ and for different values of Ma ; the Mach number takes the values $Ma \approx 0$ (dotted line), $Ma = 1$ (solid line), $Ma = 2$ (dashed line) and $Ma = 5$ (dash-dotted line).

3.1. Fixed outer cylinder, $Re_2 = 0$

In principle, unstable sound waves could occur in this problem, but in practice we did not find any. In most situations, the most unstable axisymmetric modes have zero frequency, but there are exceptions to this at high Pr , detailed below.

In figure 2 we show the Reynolds number at the instability onset as a function of k for different Ma ; we define the critical Reynolds number, Re_{1c} , and corresponding wavenumber, k_c , as the minimum of Re_1 at instability onset when optimised over k . In the incompressible limit, $Ma \approx 0$, we obtain the well-known results of Rogers & Beard (1969) (see also DiPrima, Eagles & Ng 1984). By increasing gradually Ma from 0 to 5, we find that the effect of compressibility is to stabilise the system and increase the critical wavenumber k_c slightly (see table 1 below); a similar behaviour for Re_{1c} and k_c has also been observed when $Ma > 5$. This is in agreement with the analysis done by Manela & Frankel (2007). Considering fluids with constant ν and κ , rather than constant $\hat{\mu}$ and \hat{k} , does not change the behaviour of the critical point (k_c, Re_{1c}) on the curves of marginal stability significantly.

In addition to the Mach number, the compressible problem has a new dimensionless parameter, the Prandtl number, Pr . We therefore explore how the critical Reynolds number, Re_{1c} , and the critical wavenumber, k_c , vary with different Prandtl numbers. At $Ma = 1$, increasing the Prandtl number up to around 4.5 increases Re_{1c} and so stabilises the system, but the behaviour of this branch of instability, analogous to the incompressible Taylor–Couette modes, is not very different from the $Pr = 1$ case. However, beyond $Pr \approx 4.5$, the behaviour of Re_{1c} changes radically.

In figure 3 we plot, in solid line, Re_{1c} as a function of Pr at $Ma = 1$. This graph shows that different types of modes of instability have been found; in particular, between $Pr \approx 4.49$ and $Pr \approx 10.36$, the critical modes of instability are *oscillatory*, i.e. with $\omega = \text{Im}(\sigma) \neq 0$. (Owing to the symmetries of the system, critical modes of both frequencies $\pm\omega$ onset simultaneously.) This is quite remarkable as Yih (1972)

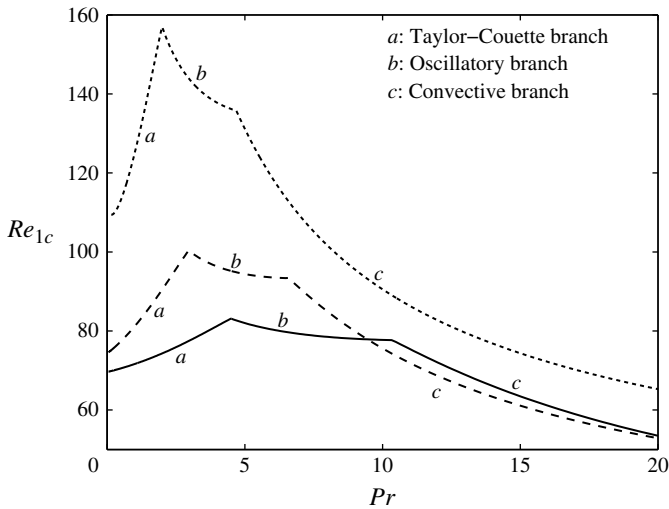


FIGURE 3. Critical Reynolds number Re_{1c} vs Pr , for $Re_2 = 0$ and $Ma = 1$ (solid line), $Ma = 2$ (dashed line) and $Ma = 5$ (dotted line). We show the Taylor–Couette branch of instability (a), the oscillatory branch (b) and the convective branch (c).

Ma	Taylor–Couette branch		Oscillatory branch			Convective branch	
	Re_{1c}	k_c	Re_{1c}	k_c	ω	Re_{1c}	k_c
1	$Pr = 1$		$Pr = 7$			$Pr = 15$	
	71.6357	3.1729	79.2450	3.1243	3.0374	63.4623	5.3778
2	$Pr = 1$		$Pr = 5$			$Pr = 10$	
	81.1803	3.1950	94.4030	3.1094	4.6189	75.5901	5.4300
5	$Pr = 1$		$Pr = 3$			$Pr = 10$	
	125.0028	3.2457	143.6191	3.1549	7.8603	90.5228	5.6478

TABLE 1. Typical values of Re_{1c} and k_c for the three different branches of instability, when the outer cylinder is at rest.

proved that there could be no unstable oscillatory modes with $m = 0$ in incompressible Couette flows. So, the appearance of a Hopf bifurcation is a specifically compressible effect. For $Pr > 10.36$ a new type of steady mode, which we identify below as a convective mode, takes over; it has a much higher wavenumber ($k_c \gtrsim 5$) at onset. The three different branches of instability identified continue to exist, for a range of values of Pr , when they are no longer the critical mode. As expected, the frequency of the oscillatory modes tend to zero when Pr tends to values where this branch ceases to exist. Interestingly, whereas the Taylor–Couette modes are stabilised by increasing the Prandtl number, for the oscillatory branch of instability, Re_{1c} diminishes as Pr increases. The reduction of Re_{1c} with increasing Pr is even more pronounced for convective modes, inasmuch as the smallest values of Re_{1c} are achieved by these modes at large Pr . In the region $Pr \gtrsim 20$, $Ma \gtrsim 5$ of the parameter space the Knudsen number satisfies $Kn \propto Ma/Re_1 \gtrsim 10^{-1}$. Therefore kinetic effects may lead to velocity slip and temperature jump at the walls, which are not modelled by our choice of boundary conditions (Manela & Frankel 2007).

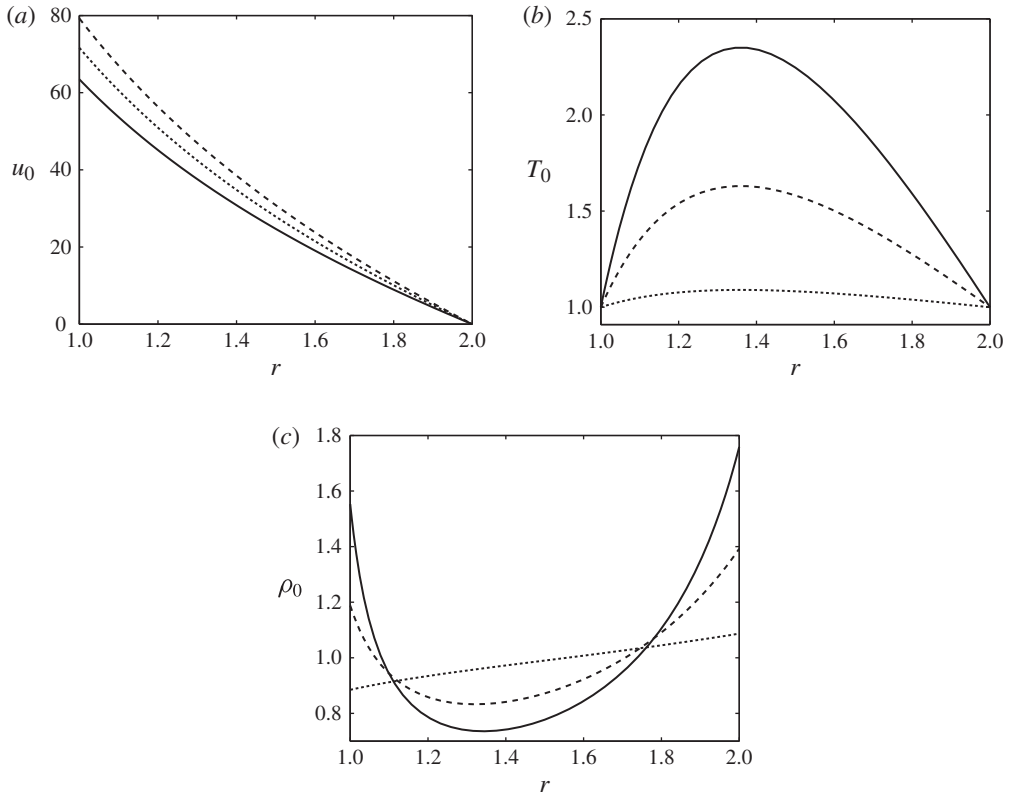


FIGURE 4. Basic state profiles of velocity (a), temperature (b) and density (c) for different values of Pr , with $Ma = 1$, $Re_2 = 0$ and Re_1 close to critical. The case $Pr = 1$ with $Re_{1c} \approx 71.64$ is shown in dotted line, $Pr = 7$ with $Re_{1c} \approx 79.24$ in dashed line and $Pr = 15$ with $Re_{1c} \approx 63.46$ in solid line.

The plots in dashed and dotted lines in figure 3 show that similar regimes of instability occur for higher Ma , the main difference being that the range of Pr leading to oscillatory modes is reduced and shifted towards lower Pr (critical modes are oscillatory between $Pr \approx 2.96$ and $Pr \approx 6.59$ at $Ma = 2$, and between $Pr \approx 1.99$ and $Pr \approx 4.69$ at $Ma = 5$; they become convective at larger Pr). Hence, convective modes can become dominant at smaller Pr when Ma is sufficiently large. We see in figure 3 that, when the Mach number changes from $Ma = 1$ to $Ma = 2$, Re_{1c} is reduced slightly for Prandtl numbers from $Pr \approx 10.36$ to $Pr \gtrsim 20$; note however that all three types of modes of instability, Taylor–Couette, oscillatory and convective, are stabilised by compressible effects at large Ma .

Some insight into the new branches of instability may be gained from examining the changes to the basic state. So, in figure 4 we show basic states at $Ma = 1$ and for parameter values where the three different types of instability onset: a Taylor–Couette mode in dotted line, an oscillatory mode in dashed line and a convective mode in solid line. Since viscous heating is generated in these differentially rotating flows, the temperature profile depends crucially on viscosity and thermal conductivity. Figure 4(b) shows that the temperature in the bulk of the fluid increases with the Prandtl number; the maximum temperature varies from $T \approx 1.1$ at $Pr = 1$ to $T \approx 1.6$

at $Pr = 7$ and $T \approx 2.4$ at $Pr = 15$. Large temperature gradients, which develop at high Prandtl number, have an important impact on the fluid density stratification. When $Pr = 1$ the temperature does not vary significantly with the radius and thus the density profile shown in figure 4(c), slightly increasing outwards, is essentially determined by the balance between pressure and centrifugal forces. But, at $Pr = 7$, the fluid, hotter near the mid-radius than at the boundaries, expands and creates a depletion of material locally. By conservation of mass, fluid removed from the centre accumulates near the boundaries. Thus, a negative density gradient forms near the inner cylinder, in the presence of an effective gravity pointing outwards, which corresponds to the centrifugal force acting on the fluid in rotation. This configuration is analogous to the setup leading to Rayleigh–Taylor instabilities when heavy fluid stands on top of lighter fluid and gravitation points downwards. Near the outer cylinder, the density gradient is positive, giving a stable stratification there. The stable stratification has the potential to give rise to waves analogous to gravity waves. In figure 4(c), the negative density gradient observed at the inner radius at $Pr = 7$ becomes larger at $Pr = 15$, and the density is also higher at the outer radius.

The critical Reynolds numbers, corresponding wavenumbers and, where non-zero, the frequencies at some typical parameter values are given in table 1. We note that the frequencies of the oscillatory modes are much smaller than those of sound waves, since in these units the isothermal sound speed is Re_1/Ma . In figure 5 we show the eigenfunctions corresponding to the different types of unstable mode, all at $Ma = 1$, at the parameter values given in the top row of table 1. In the incompressible limit, as the Mach number tends to zero, the differentially rotating flow between the cylinders becomes neutrally stable for $Re_{1c} \approx 68.19$, and steady ($\omega = 0$) Taylor–Couette cells form with a critical wavenumber $k_c \approx 3.16$. Figure 5(a) shows that, when compressible effects are considered, at $Ma = 1$, with $Pr = 1$, the formation of such Taylor–Couette cells persists, on similar length-scales, but at a higher critical Reynolds number. As seen in figure 5(d), this perturbation flow changes the fluid density. Two effects combine to modify the distribution of mass in the fluid: the divergence or convergence of the perturbation flow ($\rho_0 \nabla \cdot \mathbf{u}$) and the perturbation of the radial mass-flux ($u_r d\rho_0/dr$). At $Pr = 1$, both mechanisms are stabilising since they lead to heavy fluid moving inwards and lighter fluid moving outwards in an effective gravity field pointing towards the outer cylinder. However, at $Pr = 1$, these density fluctuations are small and do not affect the Taylor–Couette instability significantly, only increasing the critical Reynolds number somewhat.

For higher Prandtl numbers, between $Pr \approx 4.49$ and $Pr \approx 10.36$, the positive density gradient region near the outer cylinder, combined with the Taylor–Couette instability mechanism, leads to oscillatory motion at the instability onset. The flow pattern of the oscillatory mode, shown in figure 5(b), is very similar to that of the steady mode in figure 5(a), but the density perturbation, shown in figure 5(e), is now large near the outer cylinder, where the stable stratification exists. The Taylor–Couette instability is in this case destabilising the gravity waves in much the same way as a destabilising thermal stratification, acting on a stably stratified salt distribution, can excite gravity waves in the ocean. It is possible to define an effective buoyancy frequency $N = [-U_0^2/r \ln'(T_0 \rho_0^{1-\gamma})]^{1/2}$, where prime denotes a radial derivative. We have found that N is imaginary in the inner part of the flow and real in its stably stratified outer part, where density fluctuations peak (see figure 5e). The magnitude of the real part of N is of the same order of magnitude as the frequency of our oscillatory eigenfunctions, but accurate quantitative agreement is not possible. This is not surprising since the buoyancy frequency is a local concept and its derivation

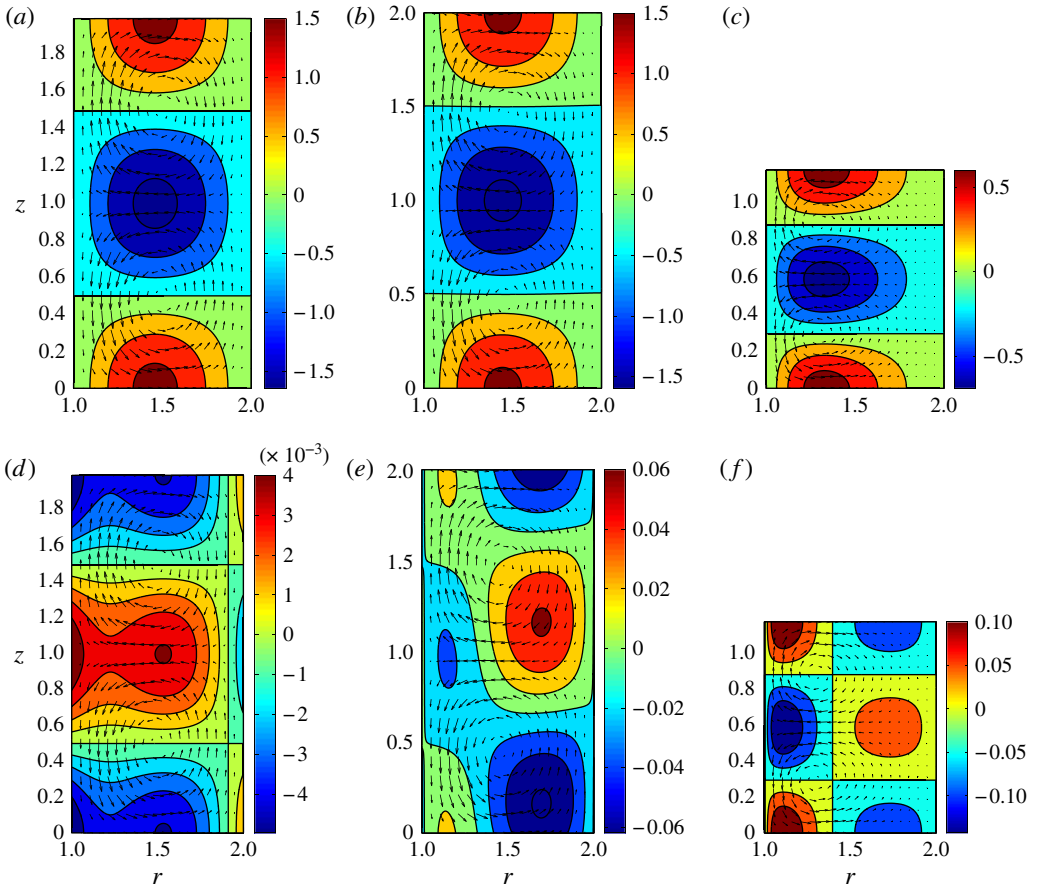


FIGURE 5. (a–c) The flow patterns at the onset of instability. The shades give u_θ and the arrows the meridional flow in the r – z plane; eigenmodes are normalised so that $\max(|u_z|) = 1$. The shade in (d–f) denotes density, and again the arrows give the meridional flow. The outer cylinder is at rest, $Ma = 1$ and (a,d) $Pr = 1$, (b,e) $Pr = 7$ and (c,f) $Pr = 15$; the corresponding values of Re_{1c} and the characteristics of the eigenmodes are given in table 1.

assumes inviscid and adiabatic processes, whereas unstable modes are global and dissipative effects are crucial.

When the Prandtl number increases further, beyond $Pr \approx 10.36$, the negative density gradient present near the inner cylinder becomes even larger and, at the instability onset, the dynamics of the fluid is now dominated by the buoyancy instability. The neutral instability cells, shown in figures 5(c,f), develop nearer to the inner cylinder – where the negative density gradient exists – and on shorter axial length scales than for the rotational instability, which is why figures 5(c) and 5(f) are shorter. In this compressible regime, at high Prandtl numbers, the critical modes are steady and of a convective nature since they are driven by an effective buoyancy instability. Here the rotational instability plays essentially a limiting role in the development of the convective instability.

Interestingly, buoyancy, and hence convective instabilities, can be enhanced or reduced by varying the basic state temperature distribution between the cylinders; this

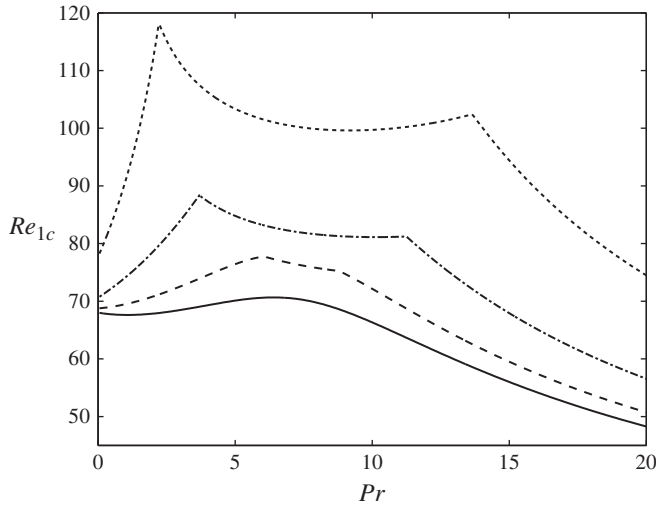


FIGURE 6. Critical Reynolds number Re_{1c} vs Pr , for $Re_2 = 0$, $Ma = 1$ and the outer cylinder temperature $\chi = 0.5, 0.9, 1.1$ and 1.2 in dotted, dash-dotted, dashed and solid line respectively.

should therefore affect the range of Pr corresponding to the different critical branches of instability. Variations of the wall temperature were present in the experiment of Larignon *et al.* (2006). Figure 6 shows the consequences of varying the temperature of the outer cylinder; $\chi < 1$ (resp. $\chi > 1$) corresponds to the case of the temperature on the outer cylinder being lower (resp. higher) than that on the inner one. Hence decreasing χ should stabilise the fluid stratified by an effective gravity pointing radially outwards. As expected, when χ varies from 1 (solid line in figure 3) to 0.5, the critical Reynolds number increases for all Pr ; conversely, when χ varies from 1 to 1.2, Re_{1c} is reduced. In addition we have found that the lower bound of the range of Prandtl numbers leading to convective modes at instability onset decreases with increasing χ ; critical modes are of a convective nature when $Pr \gtrsim 13.65$ for $\chi = 0.5$; when $Pr \gtrsim 11.24$ for $\chi = 0.9$; and when $Pr \gtrsim 8.80$ for $\chi = 1.1$. Simultaneously, the upper bound of the range of Prandtl numbers producing centrifugal modes at instability onset increases with χ ; critical modes are centrifugal when $Pr \lesssim 2.22$ for $\chi = 0.5$; when $Pr \lesssim 3.69$ for $\chi = 0.9$; and when $Pr \lesssim 6.04$ for $\chi = 1.1$. Therefore the interval of Pr giving oscillatory modes at onset shrinks when the outer cylinder gets hotter. In fact, when $\chi = 1.2$ we have found steady modes at instability onset for all Prandtl numbers: the oscillatory branch still exists, over a narrow range of Pr , but only at Reynolds numbers above critical. This shows that the centrifugal branch of instability merges with the branch of convective instability as χ is increased. When $\chi = 1$ the centrifugal and convective branches are distinct, but when $\chi = 1.1$ the two branches have merged to form a single branch of instability. However at $\chi = 1.1$ for the range $6.04 \lesssim Pr \lesssim 8.80$ the oscillatory mode is preferred, though at higher χ the merged centrifugal-convective branch dominates. Interestingly, the critical Reynolds number for this convective branch is a slowly varying function of the Prandtl number, for small Pr .

By adjusting the wall temperature ratio χ downwards, it is therefore possible to see all the possible modes of instability (centrifugal, oscillatory and convective) even for fluids with Prandtl numbers around unity.

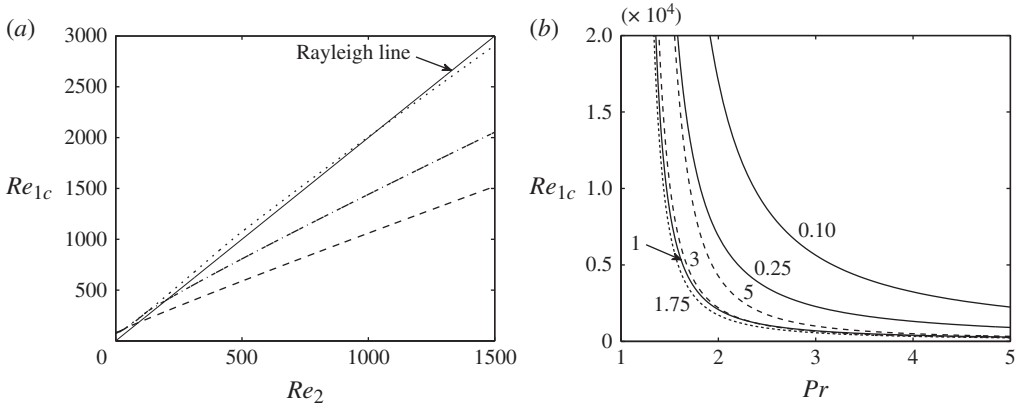


FIGURE 7. (a) Stability curves, Re_{1c} vs Re_2 , for $Ma=1$ and $Pr=7, 4$ and 2 , in dashed, dash-dotted and dotted line respectively; the solid line indicates the Rayleigh line, $Re_1 = Re_2/\eta$. (b) Critical Reynolds number Re_{1c} , on the Rayleigh line $Re_2 = \eta Re_{1c}$, as a function of Pr for a series of values of Ma between 0.1 and 5 , as indicated.

3.2. Crossing of the Rayleigh line

We now consider the case where both inner and outer cylinders rotate in the same direction. It is well-known that, in the incompressible regime, linear instability only occurs when the angular momentum in the basic state flow decreases outwards, i.e. when $Re_2 < \eta Re_1$ in our nondimensional units (see e.g. Chandrasekhar 1961). Very unexpectedly we found that, for compressible flows, instability can occur even when the Reynolds numbers Re_1 and Re_2 lie below the Rayleigh line $Re_1 = Re_2/\eta$.

In figure 7(a) we show a series of stability curves, Re_{1c} against Re_2 , for $Ma = 1$. At $Pr = 7$, an oscillatory mode onsets first when the outer cylinder is at rest (see also figure 3) and, as Re_2 increases, the critical modes remain oscillatory until $Re_2 \approx 43$, when convective modes become the most unstable. Since these convective modes are not driven by centrifugal instability, they do not respect the Rayleigh line, and we find that this branch of instability crosses the Rayleigh line at $Re_2 \approx 90$. For smaller Prandtl numbers, as Re_2 increased we again observed similar changes in the nature of the critical modes of instability as well as the crossing of the Rayleigh line by the convective branch, but for larger Reynolds numbers. At $Pr = 4$, for $0 \leq Re_2 < 7$, steady Taylor–Couette modes of instability onset first. However, for larger Re_2 , gravity waves are destabilised so that the critical modes become oscillatory, until $Re_2 \approx 128$ when convective modes take over. The crossing of the Rayleigh line then occurs at $Re_2 \approx 201$. For $Pr = 2$, at the onset of instability, steady Taylor–Couette modes are preferred for $0 \leq Re_2 < 63$, oscillatory modes for $63 \leq Re_2 < 484$ and convective modes beyond. The convective branch intersects the Rayleigh line at $Re_2 \approx 1040$.

We notice in figure 7(a) that, as Pr decreases from 7 to 2 , the critical curve for the convective branch tends to become parallel to the Rayleigh line. This demonstrates that a reduction of the maximum temperature in the bulk of the fluid, resulting from a diminution of Pr , leads to the stabilisation of the radial stratification. In fact, we found that the underlying physical mechanism giving rise to convective instabilities differs depending on the value of Pr . The convective modes found are the consequence of an unstable stratification of the fluid between the cylinders which can result from an unstable mass distribution (a form of Rayleigh–Taylor instability) or from an unstable

temperature profile (thermal convection). At $Pr = 7$ and $Pr = 4$, for the range of Reynolds numbers shown in figure 7(a), the mass distribution always presents an unstable (negative) gradient near the inner boundary, driving convective instabilities as previously discussed (see e.g. figure 4c). However, at $Pr = 2$, the mass density increases monotonically with the radius, for all basic state flows at instability onset. We can nevertheless demonstrate that, at $Pr = 2$, the temperature profile still makes the fluid unstably stratified, by examining the basic state entropy, $s \propto \ln(T_0 \rho_0^{1-\gamma})$, which presents a positive (and hence unstable) gradient near the inner boundary. For Reynolds numbers on the Rayleigh line at the instability onset, the magnitude of the unstable entropy gradient decreases with decreasing Pr and, simultaneously, the extent of the unstably stratified region shrinks. These properties of the basic state illustrate the stabilisation of the radial stratification and the localisation of the critical modes at low Pr . Moreover, for all critical modes on the Rayleigh line, the velocity perturbations are confined to meridional planes, i.e. $u_\theta = 0$.

In figure 7(b) we see very rapid increases in critical Reynolds numbers around values of Pr that depend on Ma . For instance, at $Ma = 1$, on the Rayleigh line, thermal convection onsets at $Re_{1c} \approx 2080.75$ and $k_c \approx 11.44$ when $Pr = 2$ and at $Re_{1c} \approx 139\,164.01$ and $k_c \approx 52.85$ when $Pr = 1.2$. Interestingly, we found that there is an optimal value of Ma which minimises Re_{1c} for all the values of Pr considered. Increasing the fluid compressibility from incompressible to $Ma \approx 1.75$ reduces the critical Reynolds number for the convective modes crossing the Rayleigh line (see solid lines in figure 7b). However, above this threshold, shown by a dotted line in figure 7(b), increasing the Mach number stabilises the radial stratification (see dashed lines).

Most of the results discussed in this section hold whether $\hat{\mu}$ and \hat{k} , or ν and κ , are assumed constant. In both regimes of dissipation we have found the same branches of modes at instability onset (centrifugal, oscillatory and convective), with the convective branch leading to the violation of Rayleigh’s criterion. The regions of the parameter space where the various types of modes exist vary in both regimes however. For instance, when ν and κ are constant, no value of the Prandtl number has been found (with $\chi = 1$) where oscillatory modes onset first for $Re_2 \lesssim 10$. In this regime, convective modes seems generally dominating, leading in particular to the breaking of Rayleigh’s criterion at significantly smaller Reynolds numbers than when $\hat{\mu}$ and \hat{k} are constant (all other parameters being fixed).

4. Counter-rotating cylinders

In this section, we discuss the stability of compressible Taylor–Couette flows with counter-rotating cylinders, for which we have taken $Re_1 > 0$ and $Re_2 < 0$. We investigated the impact of changing Ma and Pr on the stability of axisymmetric (steady) modes and of non-axisymmetric (oscillatory) modes with $m = 1$, which are known to be important in the case of counter-rotating cylinders, for incompressible flows (see, e.g., Davey *et al.* 1968; Chossat & Iooss 1994). Critical values of the Reynolds numbers are referred to as Re_{1c}^0 and Re_{1c}^1 , for modes $m = 0$ and $m = 1$ respectively. We define the difference between the critical Reynolds numbers to be $\Delta = Re_{1c}^1 - Re_{1c}^0$, so that Δ is negative when non-axisymmetric instabilities are preferred. The case $\Delta = 0$ is a codimension 2 point, as discussed below, corresponding to the simultaneous onset of one axisymmetric and one non-axisymmetric mode of instability. A nonlinear analysis is then required to elucidate the behaviour of the fluid at the onset of instability.

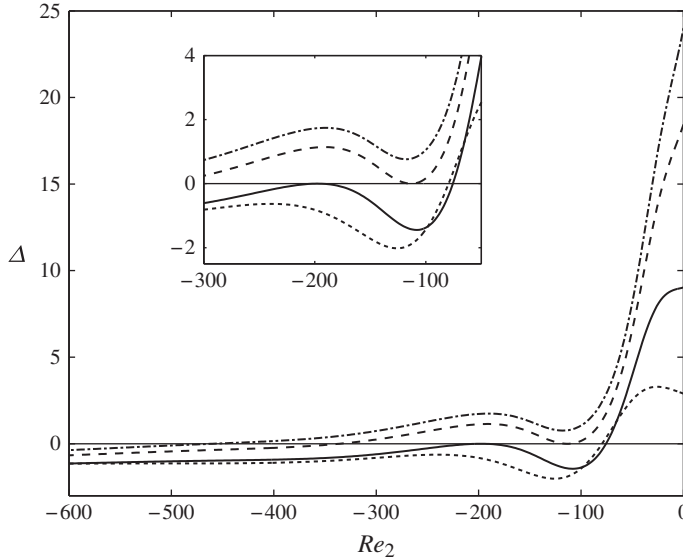


FIGURE 8. Difference between the critical Reynolds number for the modes $m = 0$ and $m = 1$, $\Delta = Re_{1c}^1 - Re_{1c}^0$, plotted against Re_2 for incompressible flows and for different values of η . The radius ratio takes the values $\eta = 1/3$ (dash-dot line), $\eta \approx 0.3630$ (dashed line), $\eta \approx 0.4632$ (solid line) and $\eta = 2/3$ (dotted line).

4.1. The incompressible case

Firstly we wish to review, in this framework, results from the incompressible regime, corresponding to $Ma \approx 0$. In figure 8, we plot Δ against Re_2 for different radius ratios η . For all values of η , non-axisymmetric instability is preferred provided that Re_2 is sufficiently negative. However, for $\eta = 1/3$ and $\eta = 2/3$, a crossing of the axis $\Delta = 0$ occurs, which means that the axisymmetric instability is preferred below a certain value of $|Re_2|$.

At $\eta = 1/3$, as Re_2 decreases the value of Δ goes through a local minimum at $Re_2 \approx -118$, followed by a local maximum at $Re_2 \approx -190$, subsequently falling and crossing the $\Delta = 0$ axis at $Re_2 \approx -460$. As we gradually increase η from $1/3$, the local minimum of Δ approaches the $\Delta = 0$ axis, which it touches at $\eta \approx 0.363$, $Re_2 \approx -113.19$ and $Re_1 \approx 113.12$. This point is therefore a codimension 3 point where the parameters η , Re_1 and Re_2 all have particular values. If one lets σ^0 and σ^1 (both functions of k , Re_1 , Re_2 and η) be the growth rates of the modes $m = 0$ and $m = 1$ respectively, then, at a critical point of the $m = 0$ mode, $\sigma^0 = \partial\sigma^0/\partial k = 0$. Solving these equations determines $k_c^0(Re_2, \eta)$ and $Re_{1c}^0(Re_2, \eta)$. Similarly, for the $m = 1$ mode, we obtain $k_c^1(Re_2, \eta)$ and $Re_{1c}^1(Re_2, \eta)$. A codimension 2 point satisfies the additional equation $Re_{1c}^0(Re_2, \eta) = Re_{1c}^1(Re_2, \eta)$, or equivalently $\Delta = 0$, which, for given η , determines Re_2 . At a codimension 3 point the further equation $\partial Re_{1c}^0/\partial Re_2 = \partial Re_{1c}^1/\partial Re_2$, or $\partial\Delta/\partial Re_2 = 0$, must hold and thus determines η uniquely.

As η is increased above 0.363 , the local minimum goes below the $\Delta = 0$ axis, so there are now three codimension 2 points. The local maximum, located between the codimension 2 points with the most negative Re_2 values, comes down and touches the $\Delta = 0$ axis to give a second codimension 3 point at $\eta \approx 0.4632$, $Re_2 \approx -197.65$ and $Re_1 \approx 144.08$. Further increasing η reduces the number of codimension 2 points

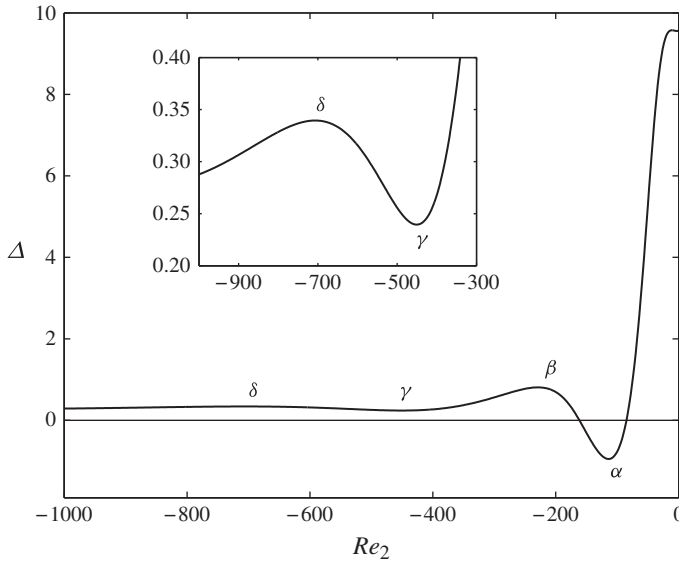


FIGURE 9. Difference between the critical Reynolds number for the modes $m = 0$ and $m = 1$, $\Delta = Re_{1c}^1 - Re_{1c}^0$, plotted against Re_2 , at $Ma = 2$ and $Pr = 1$. Four turning points of the curve, occurring successively for increasing values of $|Re_2|$, are labelled α , β , γ and δ respectively.

back to one and there are no further codimension 3 points. The codimension 3 points described above have also been observed by Signoret & Iooss (1988) (see also Signoret 1988).

4.2. The compressible case

We now revert back to the case when $\eta = 0.5$ and investigate the effects of compressibility on counter-rotating Taylor–Couette flows.

Figure 9, presenting Δ as a function of Re_2 at $Ma = 2$ and $Pr = 1$, shows that axisymmetric modes are preferred when the outer cylinder is a rest; this remains true until $|Re_2|$ reaches values where Δ becomes negative, in which case $m = 1$ modes onset first. As $|Re_2|$ is increased further, the curve Δ crosses the $\Delta = 0$ axis for a second time and remains above for $Re_2 \geq -10^3$, thus demonstrating the prevalence of axisymmetric modes for a large range of Reynolds numbers. We believe however that Δ crosses the $\Delta = 0$ axis again, at $|Re_2|$ significantly greater than 10^3 (not computed), so that $m = 1$ modes are ultimately preferred.

Similarly to the incompressible case, the graph of Δ against Re_2 , as shown in figure 9, presents a series of local maxima and minima, but compressibility typically introduces additional turning points. Changes in the sign of these local extrema, as a parameter varies, indicate the emergence or coalescence of a pair of codimension 2 points, where modes $m = 0$ and $m = 1$ onset simultaneously. The sign of successive turning points of Δ , fixing the number of crossings of the $\Delta = 0$ axis or codimension 2 points (always odd), determines the number of intervals of Re_2 where modes of a given symmetry are preferred. Figure 10 illustrates this behaviour of the system when $Pr = 1$ and Ma varies. For values of Ma between 0 and ≈ 0.74 , only one crossing of the $\Delta = 0$ axis has been found, so axisymmetric modes are preferred above a critical

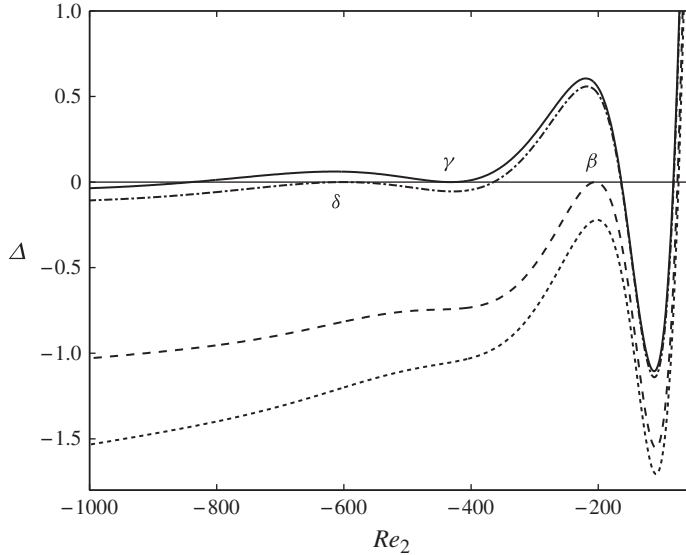


FIGURE 10. The same as in figure 9 but for different Mach numbers: the curves shown by dotted, dashed, dash-dotted and solid lines correspond to $Ma \approx 0, 0.7412, 1.6074$ and 1.6780 respectively. Codimension 3 points are denoted using labels of turning points touching the horizontal axis, as defined in figure 9.

Re_2 and $m = 1$ modes below. When $Ma \approx 0.74$, the local maximum Δ_β (value of Δ named after turning point labels as defined in figure 9) becomes zero; this is a codimension 3 point, as discussed in §4.1, with Ma replacing the parameter η . As Ma increases further two additional codimension 2 points appear; hence two intervals of Re_2 leading to $m = 1$ modes at instability onset are interspersed with two regions where $m = 0$ modes are preferred, until $Ma \approx 1.61$ when another local maximum, Δ_δ , becomes zero. This determines a second codimension 3 point. For a narrow range of Ma , from ≈ 1.61 to ≈ 1.68 , we found five codimension 2 points, so that three intervals of Re_2 where $m = 1$ modes are preferred straddle three regions where modes are axisymmetric at the instability onset. The point where the local minimum $\Delta_\gamma = 0$, obtained for $Ma \approx 1.68$, is a third codimension 3 point; beyond this value of Ma the number of crossings of the $\Delta = 0$ axis is reduced back down to three. For $Pr = 1$ we have not attempted to compute a fourth codimension 3 point, which would have to satisfy the condition $\Delta_\alpha = 0$, as the Mach number involved would be too large.

Figure 11 presents the displacement of codimension 3 points as Ma and Pr vary in a consistent manner allowing us to follow these points. We focus on two turning points of the curve (Re_2, Δ) , namely the local maximum δ , defined in figure 9, and a local minimum labelled ε , which could not be seen for $Ma = 2$ and $|Re_2| \leq 10^3$. (Notice that the presence of the local minimum ε suggests the existence of another local maximum at higher $|Re_2|$.) At $Ma = 1$, the codimension 3 point defined by $\Delta_\delta = 0$ is located on the curve a_δ around $Re_2 = -544$ and that defined by $\Delta_\varepsilon = 0$ at a higher Reynolds number (in absolute value), $Re_2 \approx -829$, on the curve a_ε . When Ma decreases from 1 to 0.6, the turning points δ and ε get closer to one another; as seen on the curves b_δ and b_ε these codimension 3 points are now found at $Re_2 \approx -569$ and $Re_2 \approx -676$ respectively. Interestingly, as Ma tends to 0.51 and Pr approaches 1.97, the local maximum δ and the local minimum ε merge to form a horizontal

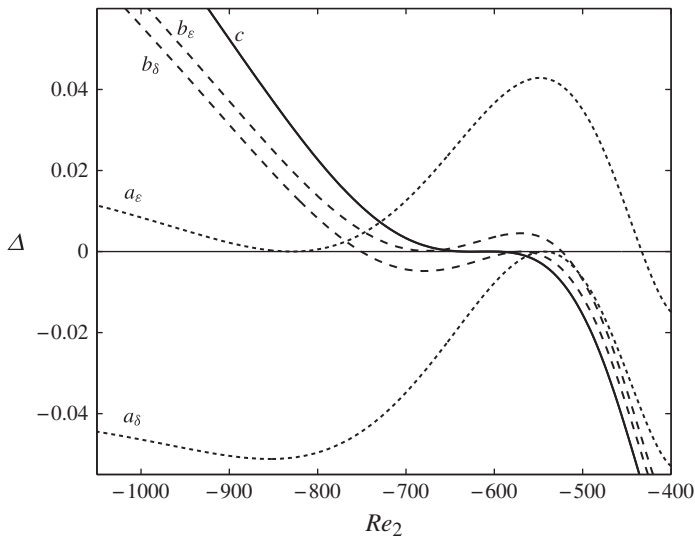


FIGURE 11. The same as in figure 9 but for different Ma and Pr . Three families of curves, denoted by a , b and c (dotted, dashed and solid lines), have been obtained for $Ma = 1$, 0.6 and 0.51 respectively. Each curve a and b possesses a local maximum, labelled δ (see figure 9), and a local minimum, labelled ε . When δ touches the horizontal axis it is a codimension 3 point, as on a_δ and b_δ for which $Pr \approx 1.336$ and 1.792 respectively; on a_ε and b_ε , for which $Pr \approx 1.357$ and 1.794 respectively, ε touches the horizontal axis and is therefore also a codimension 3 point. The curve c , which has a horizontal inflexion point on the horizontal axis, was obtained for $Pr \approx 1.970$.

inflexion point on the $\Delta = 0$ axis, visible on the curve c . This means that the two codimension 3 points coalesce in a codimension 4 point, where both parameters Ma and Pr are uniquely determined by the conditions $\partial\Delta/\partial Re_2 = \partial^2\Delta/\partial Re_2^2 = 0$. At the codimension 4 point $Re_2 \approx -620$; the actual value of the Reynolds number is however difficult to calculate accurately, owing to the limited variation in Δ for a range of Re_2 near the codimension 4 point.

In the more general case when Re_2 , Ma and Pr are considered as independent parameters (η being kept fixed), the condition $\Delta = 0$ can again be used, as discussed in §4.1, to determine Re_2 , say, as a function of Ma and Pr , at a codimension 2 point. At a codimension 3 point, the further equation $\partial\Delta/\partial Re_2 = 0$ then defines a relationship between Ma and Pr that can be represented as a continuous curve in the (Pr, Ma) -plane. Such curves are plotted in the regime diagram in figure 12, for codimension 3 points which coincide with the turning points α – ε (see figures 9 and 11). The different lines shown bound regions of space where the system possesses a fixed number of codimension 2 points. This diagram is however incomplete since at least one codimension 3 point, occurring at a local maximum of Δ which must exist beyond the turning point ε (i.e. at larger $|Re_2|$), is missing. Nevertheless, one can see in figure 12(a) that only one codimension 2 point exists above the curve α and below the curve β . In the region of parameter space banded by the dotted and dash-dot lines, the number of codimension 2 points has been found to vary between 3 and 5. It may seem that the line δ terminates abruptly but in fact figure 12(b) shows that it intersects the line ε to form a cusp. This demonstrates how the two

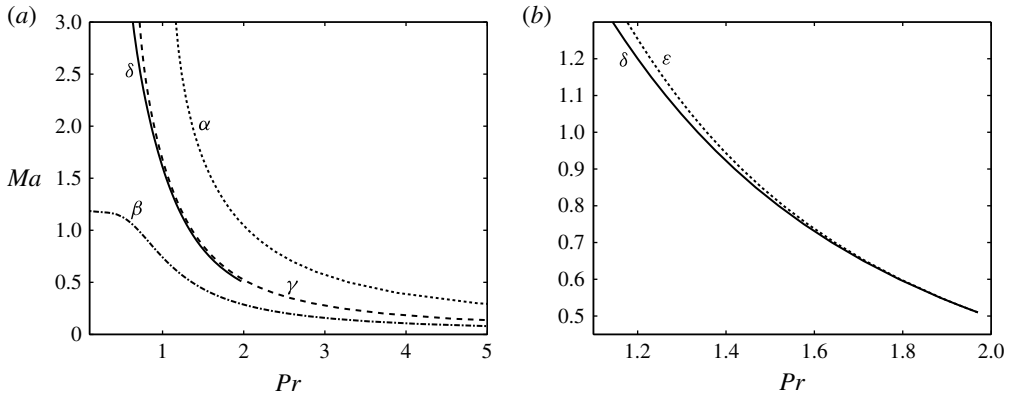


FIGURE 12. Regime diagram showing the location of codimension 3 points in the (Pr – Ma) plane. (a) Four lines, bounding different regimes of instability, consist of codimension 3 points which follow maxima (β in dash-dotted line and δ in solid line) and minima (α in dotted line and γ in dashed line) defined in figure 9. (b) Two lines now follow the maximum, δ in solid line, and minimum, ϵ in dotted line, defined in figure 11.

codimension 3 points δ and ϵ coalesce in a codimension 4 point as Ma decreases (or equivalently as Pr increases).

5. Discussion and conclusions

In this paper, we have studied the linear Taylor–Couette problem for a compressible fluid. We have modelled the flow of a perfect gas in the continuum limit and thus kinetic effects, which may affect both the boundary conditions and the form of the transport coefficients, have been ignored. This level of approximation is valid as long as the Knudsen number, $Kn \sim Ma/Re_1$, remains sufficiently small. Yoshida & Aoki (2006) and Manela & Frankel (2007) have shown that, in a limited region of the parameter space, slight rarefaction ($Kn \sim 0.01$) can stabilise the system. It would therefore be of great interest to re-examine, in subsequent work, the dynamical effects revealed by our analysis, in the framework of rarefied gas dynamics, by using appropriate kinetic models. Here, we have primarily investigated the effect of changing the Mach number and the Prandtl number of the fluid flow, for both axisymmetric and asymmetric modes of instability.

When the outer cylinder is held fixed, axisymmetric instabilities onset first. For $Pr=1$ or less, we found that increasing Ma does have a stabilising effect, confirming the results of Manela & Frankel (2007). As they pointed out, it is important to solve for the basic state temperature and density in a way which leaves the total mass of gas unchanged as external parameters such as Re_1 , Re_2 and Ma are varied.

At larger values of Pr , previously unknown behaviour occurs due to compressibility. Axisymmetric oscillatory modes, and steady convective modes can occur, in addition to the classical rotationally driven Taylor–Couette modes. Physically, these new modes arise because of the viscous heating occurring in the basic state. At high Prandtl number, the heat generated by the viscous shear cannot escape quickly, and so the temperature rises significantly in the middle of the gap. At moderate gap widths the centrifugal acceleration provides an effective radial gravity, so the density variations consequent on the shear heating can give rise to either stabilising

or destabilising radial density gradients. In the case of a stabilising radial density gradient, internal gravity waves can be destabilised by the shear, leading to oscillatory modes of instability. When the density gradient is destabilising, we have the possibility of Rayleigh–Taylor instability, which can occur even when the angular momentum increases outward everywhere. The classical Rayleigh criterion for instability therefore no longer applies, and instability can be found below the Rayleigh line. Even when the density gradient increases outwards, if there is an unstable entropy gradient, thermal convection, rather than Rayleigh–Taylor instability, can occur.

Our physical explanation of the instability is supported by the nature of the eigenfunctions of the various modes. Modes driven by Rayleigh–Taylor or thermal convection are located mainly in the regions where the basic state gradient is most unstable. Note that for very narrow gaps, the centrifugal acceleration u_0^2/r becomes small, so we would not expect these instability mechanisms to occur for very narrow gaps, i.e. η close to unity. For inner and outer cylinders at the same fixed temperature, we only found these new instability mechanisms at Prandtl numbers greater than unity, whereas most simple gases have Prandtl numbers slightly less than unity. To see these mechanisms in the laboratory, it will be necessary to adjust the temperature boundary conditions, so that the outer cylinder is slightly warmer than the inner cylinder, to enhance the instability of the basic state density and entropy gradients. Preliminary estimations show for instance that it is possible to violate Rayleigh’s criterion for air ($Pr = 0.7$) at $Re_{1c} \simeq 452$ if the temperature of the outer cylinder is increased by 20%. In astrophysical situations, sheared magnetic fields can lead to ohmic heating, and this might also destabilise Couette flow in a way similar to that found here.

We have also considered the counter-rotating case. The interest here is not so much in the high Prandtl number instabilities, but mainly in the interaction between the axisymmetric $m = 0$ mode and the non-axisymmetric $m = 1$ mode. The existence of a codimension 2 point where these onset simultaneously has long been known in the Boussinesq case. Less well-known, but verified by our studies, is the existence of Boussinesq codimension 3 points at radius ratios $\eta \approx 0.363$ and $\eta \approx 0.463$. Our exploration of the compressible case shows that codimension 3 points can occur for a range of radius ratios at particular values of the Mach number. Indeed, the nature of these compressible bifurcation points is remarkably complex, with many different possibilities of codimension 3 bifurcations available. It remains to see what nonlinear behaviour emerges from these complex bifurcations.

Acknowledgements

The authors are grateful to anonymous referees for comments that have improved the manuscript. S.W. was supported by the UK’s Science and Technology Facilities Council (STFC) under Studentship ST/H002332/1; C.A.J. and E.K. are supported by STFC under Consolidated Grant ST/K000853/1.

Appendix A. The governing non-dimensional linear equations

On assuming a normal mode solution, in which all variables take the form $\exp[\sigma t + i(m\theta + kz)]$, and denoting perturbations to the density, velocity and temperature by ρ , $\mathbf{u} = (u_r, u_\theta, u_z)$ and T respectively, the equations governing the linear perturbations, derived from (2.7) to (2.9), may be expressed as:

$$\sigma \rho = -im \frac{u_0}{r} \rho - \frac{1}{r} \frac{d}{dr} (r \rho_0) u_r - \rho_0 \frac{du_r}{dr} - im \frac{\rho_0}{r} u_\theta - ik \rho_0 u_z, \tag{A 1}$$

$$\begin{aligned} \sigma u_r = & \frac{Re_1^2 T_0}{Ma^2 \rho_0^2} \frac{d\rho_0}{dr} \rho - \frac{Re_1^2 T_0}{Ma^2 \rho_0} \frac{d\rho}{dr} - \left[\frac{1}{\rho_0} \left(\frac{4}{3r^2} + \frac{m^2}{r^2} + k^2 \right) + im \frac{u_0}{r} \right] u_r \\ & + \frac{4}{3r\rho_0} \frac{du_r}{dr} + \frac{4}{3\rho_0} \frac{d^2 u_r}{dr^2} + \left(2 \frac{u_0}{r} - \frac{7im}{3r^2 \rho_0} \right) u_\theta + \frac{im}{3r\rho_0} \frac{du_\theta}{dr} \\ & + \frac{ik}{3\rho_0} \frac{du_z}{dr} - \frac{Re_1^2}{Ma^2 \rho_0} \frac{d\rho_0}{dr} T - \frac{Re_1^2}{Ma^2} \frac{dT}{dr}, \end{aligned} \quad (A 2)$$

$$\begin{aligned} \sigma u_\theta = & -im \frac{Re_1^2 T_0}{Ma^2 r \rho_0} \rho - \left[\frac{1}{r} \frac{d}{dr} (ru_0) - \frac{7im}{3r^2 \rho_0} \right] u_r + \frac{im}{3r\rho_0} \frac{du_r}{dr} \\ & - \left[\frac{1}{\rho_0} \left(\frac{1}{r^2} + \frac{4m^2}{3r^2} + k^2 \right) + im \frac{u_0}{r} \right] u_\theta + \frac{1}{r\rho_0} \frac{du_\theta}{dr} \\ & + \frac{1}{\rho_0} \frac{d^2 u_\theta}{dr^2} - \frac{mk}{3r\rho_0} u_z - im \frac{Re_1^2}{rMa^2} T, \end{aligned} \quad (A 3)$$

$$\begin{aligned} \sigma u_z = & -ik \frac{Re_1^2 T_0}{Ma^2 \rho_0} \rho + \frac{ik}{3r\rho_0} u_r + \frac{ik}{3\rho_0} \frac{du_r}{dr} - \frac{mk}{3r\rho_0} u_\theta \\ & - \left(\frac{m^2}{r^2 \rho_0} + \frac{4k^2}{3\rho_0} + im \frac{u_0}{r} \right) u_z + \frac{1}{r\rho_0} \frac{du_z}{dr} + \frac{1}{\rho_0} \frac{d^2 u_z}{dr^2} - ik \frac{Re_1^2}{Ma^2} T, \end{aligned} \quad (A 4)$$

$$\begin{aligned} \sigma T = & - \left\{ \frac{dT_0}{dr} + (\gamma - 1) \left[\frac{T_0}{r} - 2im \frac{Ma^2}{Re_1^2 \rho_0} \frac{d}{dr} \left(\frac{u_0}{r} \right) \right] \right\} u_r - (\gamma - 1) T_0 \frac{du_r}{dr} \\ & - (\gamma - 1) \left[2 \frac{Ma^2}{Re_1^2 \rho_0} \frac{d}{dr} \left(\frac{u_0}{r} \right) + im \frac{T_0}{r} \right] u_\theta + 2(\gamma - 1) \frac{Ma^2}{Re_1^2 \rho_0} \frac{r}{dr} \left(\frac{u_0}{r} \right) \frac{du_\theta}{dr} \\ & - ik(\gamma - 1) T_0 u_z - \left[\frac{\gamma}{Pr\rho_0} \left(\frac{m^2}{r^2} + k^2 \right) + im \frac{u_0}{r} \right] T \\ & + \frac{\gamma}{Pr\rho_0} \frac{dT}{dr} + \frac{\gamma}{Pr\rho_0} \frac{d^2 T}{dr^2}. \end{aligned} \quad (A 5)$$

This set of linear equations constitutes an eighth-order system of ordinary differential equations in r , which may be expressed as an eigenvalue problem where the eigenvalue is the complex coefficient σ . The linear system is completed by specifying eight boundary conditions derived from (2.12):

$$u_r = 0, \quad u_\theta = 0, \quad u_z = 0, \quad T = 0 \quad \text{on } r = \frac{\eta}{1 - \eta}, \quad r = \frac{1}{1 - \eta}. \quad (A 6)$$

The eigenvalue problem (A 1)–(A 6) is solved numerically, utilising the computational software MATLAB. The linear equations are discretised and written in matrix form by means of a Chebyshev spectral collocation method, then solved for σ using the eigenvalue solver `eig`. We seek solutions with growth rate $\text{Re}(\sigma) = 0$ and, using the optimisation function `fminbnd`, compute critical values of various control parameters.

REFERENCES

- ARMITAGE, P. J. 2011 Dynamics of Protoplanetary Disks. *Annu. Rev. Astron. Astrophys.* **49**, 195–236.
 BALBUS, S. A. & HAWLEY, J. F. 1998 Instability, turbulence, and enhanced transport in accretion disks. *Rev. Mod. Phys.* **70**, 1–53.

- CHANDRASEKHAR, S. 1961 *Hydrodynamic and Hydromagnetic Stability*. Oxford University Press.
- CHOSSAT, P. & IOOSS, G. 1994 *The Taylor–Couette Problem*, Applied Mathematical Sciences, vol. 102. Springer.
- DAVEY, A., DIPRIMA, R. C. & STUART, J. T. 1968 On the instability of Taylor vortices. *J. Fluid Mech.* **31**, 17–62.
- DIPRIMA, R. C., EAGLES, P. M. & NG, B. S. 1984 The effect of radius ratio on the stability of Couette flow and Taylor vortex flow. *Phys. Fluids* **27**, 2403–2411.
- DUBRULLE, B., DAUCHOT, O., DAVIAUD, F., LONGARETTI, P.-Y., RICHARD, D. & ZAHN, J.-P. 2005 Stability and turbulent transport in Taylor–Couette flow from analysis of experimental data. *Phys. Fluids* **17** (9), 095103.
- GOODMAN, J. & JI, H. 2002 Magnetorotational instability of dissipative Couette flow. *J. Fluid Mech.* **462**, 365–382.
- HATAY, F. F., BIRINGEN, S., ERLEBACHER, G. & ZORUMSKI, W. E. 1993 Stability of high-speed compressible rotating Couette flow. *Phys. Fluids* **5**, 393–404.
- HERSANT, F., DUBRULLE, B. & HURÉ, J.-M. 2005 Turbulence in circumstellar disks. *Astron. Astrophys.* **429**, 531–542.
- JI, H., BURIN, M., SCHARTMAN, E. & GOODMAN, J. 2006 Hydrodynamic turbulence cannot transport angular momentum effectively in astrophysical disks. *Nature* **444**, 343–346.
- KAO, K.-H. & CHOW, C.-Y. 1992 Linear stability of compressible Taylor–Couette flow. *Phys. Fluids* **4**, 984–996.
- LARIGNON, B. D., MARR, K. & GOLDSTEIN, D. B. 2006 Monte Carlo and Navier–Stokes simulations of compressible Taylor–Couette flow. *J. Thermophys. Heat Transfer* **20**, 544–551.
- MANELA, A. & FRANKEL, I. 2007 On the compressible Taylor–Couette problem. *J. Fluid Mech.* **588**, 59–74.
- PAOLETTI, M. S. & LATHROP, D. P. 2011 Angular momentum transport in turbulent flow between independently rotating cylinders. *Phys. Rev. Lett.* **106** (2), 024501.
- PAOLETTI, M. S., VAN GILS, D. P. M., DUBRULLE, B., SUN, C., LOHSE, D. & LATHROP, D. P. 2012 Angular momentum transport and turbulence in laboratory models of Keplerian flows. *Astron. Astrophys.* **547**, A64.
- ROGERS, E. H. & BEARD, D. W. 1969 A Numerical study of wide-gap Taylor vortices. *J. Comput. Phys.* **4**, 1.
- SCHARTMAN, E., JI, H., BURIN, M. J. & GOODMAN, J. 2012 Stability of quasi-Keplerian shear flow in a laboratory experiment. *Astron. Astrophys.* **543**, A94.
- SIGNORET, F. 1988 Étude de situations singulières et forçage périodique dans le problème de Couette–Taylor. PhD thesis, Université de Nice.
- SIGNORET, F. & IOOSS, G. 1988 Une singularité de codimension 3 dans le problème de Couette–Taylor. *J. Méc. Théor. Appl.* **7** (5), 545–572.
- STEFANI, F., GUNDRUM, T., GERBETH, G., RÜDIGER, G., SCHULTZ, M., SZKLARSKI, J. & HOLLERBACH, R. 2006 Experimental evidence for magnetorotational instability in a Taylor–Couette flow under the influence of a helical magnetic field. *Phys. Rev. Lett.* **97** (18), 184502.
- TAYLOR, G. I. 1923 Stability of a viscous liquid contained between two rotating cylinders. *Phil. Trans. R. Soc. Lond. A* **223**, 289–343.
- YIH, C.-S. 1972 Spectral theory of Taylor vortices part II. Proof of nonoscillation. *Arch. Rat. Mech. Anal.* **47**, 288–300.
- YOSHIDA, H. & AOKI, K. 2006 Linear stability of the cylindrical Couette flow of a rarefied gas. *Phys. Rev. E* **73** (2), 021201.